CORROSION SCIENCE AND TECHNOLOGY, Vol.22, No.6(2023), pp.399~407
[Research Paper]
pISSN 1598-6462 / eISSN 2288-6524
DOI: https://doi.org/10.14773/cst.2023.22.6.399

Investigation of Functional 6061 Aluminum Alloy Oxide Film with Anodization Voltage and its Corrosion Resistance

Jisoo Kim[1,††] and Chanyoung Jeong[1,2,†,††]

[1]*Department of Advanced Materials Engineering, Dong-eui University, Busan, 47340, Korea*
[2]*The Research Institute of Advanced Functional Surface Engineering, Busan, 47340, Korea*
(Received October 14, 2023; Revised November 10, 2023; Accepted November 11, 2023)

This study investigated the formation of oxide films on 6061 aluminum (Al) alloy and their impacts on corrosion resistance efficiency by regulating anodization voltage. Despite advantageous properties inherent to Al alloys, their susceptibility to corrosion remains a significant limitation. Thus, enhancing corrosion resistance through developing protective oxide films on alloy surfaces is paramount. The first anodization was performed for 6 h with an applied voltage of 30, 50, or 70 V on the 6061 Al alloy. The second anodization was performed for 0.5 h by applying 40 V after removing the existing oxide film. Resulting oxide film's shape and roughness were analyzed using field emission–scanning electron microscopy (FE-SEM) and atomic force microscopy (AFM). Wettability and corrosion resistance were compared before and after a self-assembled monolayer (SAM) using an FDTS (1H, 1H, 2H, 2H-Perfluorodecyltrichlorosilane) solution. As the first anodization voltage increased, the final oxide film's thickness and pore diameter also increased, resulting in higher surface roughness. Consequently, all samples exhibited superhydrophilic behavior before coating. However, contact angle after coating increased as the first anodization voltage increased. Notably, the sample anodized at 70 V with superhydrophobic characteristics after coating demonstrated the highest corrosion resistance performance.

Keywords: *Aluminum 6061 alloy, Anodization voltage variation, Corrosion resistance, Superhydrophilicity, Superhydrophobicity*

1. Introduction

In recent years, addressing global warming has prompted efforts to promote energy conservation by employing highly recyclable and cost-effective aluminum (Al) alloys in various industries, including construction, shipping, maritime, and aerospace. The 6061 Al alloy, an environmentally friendly material, has continuously improved due to its enhanced strength, formability, and corrosion resistance, achieved by adding magnesium (Mg) and silicon (Si). Despite forming a naturally thin oxide film on 6061 Al alloy upon reacting with atmospheric oxygen, providing superior corrosion resistance to other alloys, it remains susceptible to corrosion in chloride ion (Cl^-)–rich environments, such as seawater and atmospheric conditions. This susceptibility can lead to material damage, degradation, and other serious issues. Consequently, research efforts are underway to develop Al alloys with excellent corrosion resistance through various electrochemical surface treatment methods [1–4].

Among the representative methods of electrochemical surface treatment, processes like anodization and plasma electrolytic oxidation (PEO) are noteworthy. PEO enables the formation of thicker oxide films but demands high voltages, leading to significant power consumption, and has limitations in terms of pore area, restricting its applications. In contrast, anodization processes, particularly those using controlled current density, facilitate uniform and dense oxide film formation with lower voltages. Because of its cost-effectiveness and environmental friendliness, anodization is widely recognized and adopted in many industries [5–10].

Anodization involves using acidic solutions such as oxalic acid, sulfuric acid, and phosphoric acid. In this process, the metal sample to be treated is designated as the anode and subjected to a controlled voltage, resulting in oxidation reactions on the metal surface that lead to the formation of an oxide film. The process can be performed in constant current and voltage modes [11–16]. The oxide film growth is proportional to the passed charge in constant current mode. However, excessive current density can lead to "burning," causing rapid film deterioration beyond a critical current

†Corresponding author: cjeong@deu.ac.kr
††These authors contributed equally to this work as the first author.
Jisoo Kim: Graduate Student, Chanyoung Jeong: Professor

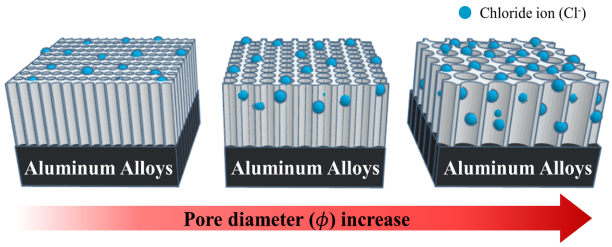

Fig. 1. Schematic diagram of penetration of corrosion-inducing substances with pore diameter of oxide film

density. On the other hand, constant voltage mode allows precise film thickness control by adjusting treatment time, ensuring consistent pore sizes and thicknesses [17–22]. The resulting oxide film exhibits various thicknesses and surface roughness. While it acts as a protective barrier against corrosive substances, the pores in structures with porous oxide films can serve as pathways for the penetration of corrosive ions, reducing corrosion resistance as pore size increases. A schematic representation of this mechanism is shown in Fig. 1 [23–29]. According to the principles illustrated in Fig. 1, increasing pore size can be mitigated by coating the surface with low surface energy materials, effectively restricting air ingress and enhancing corrosion resistance [30–38].

In this study, 6061 Al alloy was subjected to first anodization with variable voltages, followed by a second anodization process after anodic aluminum oxide (AAO) removal. The resulting oxide film structures were observed using field emission–scanning electron microscopy (FE–SEM) based on voltage variations. After measuring the surface roughness and contact angle of the final oxide film formed through the first anodization at different applied voltages, a coating was applied to the low-energy surface to compare the wetting behavior based on oxide film morphology. Furthermore, a Potentiodynamic polarization test was conducted to observe corrosion resistance.

2. Experimental Methods

In this study, the working area of 6061 Al alloy was machined into dimensions of 2.5 × 3 × 0.1 cm. The samples were subjected to ultrasonic cleaning for 10 min each in acetone and ethanol to remove surface impurities, followed by drying. Before the anodization process, a preliminary electropolishing step was conducted with a 4:1 mixture of ethanol (DUKSAN) and perchloric acid (SAMCHUN, $HClO_4$, 70%) electrolyte at 20 V for 1 min. The electropolished 6061 Al alloy was used as the anode, while platinum (Pt) was used as the cathode in a 0.3 M oxalic acid (SAMCHUN, Oxalic acid) electrolyte solution. The first anodization process was carried out for 6 h with applied voltages of 30, 50, and 70 V.

Subsequently, AAO removal was performed by immersing the samples in a mixture of 6 wt% phosphoric acid and 1.8 wt% chromic acid at 65 °C for 10 h to remove the formed oxide film and create a porous pattern. Following AAO removal, a second anodization process was conducted by applying 40 V for 0.5 h in a 0.3 M oxalic acid electrolyte, mirroring the first anodization conditions. Anodization was performed using a double-jacketed beaker maintained at 0 °C with a water-cooling system. After each step, the samples were cleaned with acetone and ethanol and dried. The thickness and pore size of the oxide film were observed and quantified using field emission–scanning electron microscopy (FE-SEM) at the Converging Materials Core Facility of Dong-eui University. The chemical composition and content of the oxide film were quantitatively analyzed using energy dispersive spectroscopy (EDS), and the surface roughness of the oxide film was measured using an atomic force microscope (AFM). EDS and AFM were used at the Converging Materials Core Facility of Dong-eui University. Surface impurities were removed using a plasma device to achieve hydrophobicity on the oxide film surface. Subsequently, the samples were dried on a hot plate at 150 °C for 10 min before being coated with a self-assembled monolayer (SAM) using FDTS (1H, 1H, 2H, 2H-Perfluorodecyltrichlorosilane) solution, a low surface energy material. To assess the hydrophilic and hydrophobic properties of the sample due to differences in pore structure resulting from variable applied voltages, the contact angle was measured using 3 μL of distilled water per sample, and the average contact angle was calculated from five measurements. Potentiodynamic polarization tests were performed in a 3.5 wt% NaCl solution to evaluate corrosion resistance before and after coating. The working electrode was the anodized sample, the counter electrode was a Pt mesh, and the reference electrode was a silver–silver chloride (Ag/AgCl) electrode. The polarization test was conducted in a three-electrode system, measuring the potential from −1.5 V to + 1.5 V at a 1 mV/s scan rate.

3. Results and Discussion

3.1 Growth of Oxide film

In this study, 6061 Al alloy was subjected to the first anodization process at variable voltages of 30, 50, and 70 V to form oxide films. The anodic oxidation reaction or oxide film growth can be explained by equation (1). Al^{3+} cations are generated at the aluminum/oxide interface, and O^{2-} or OH^- anions are formed at the oxide/solution interface.

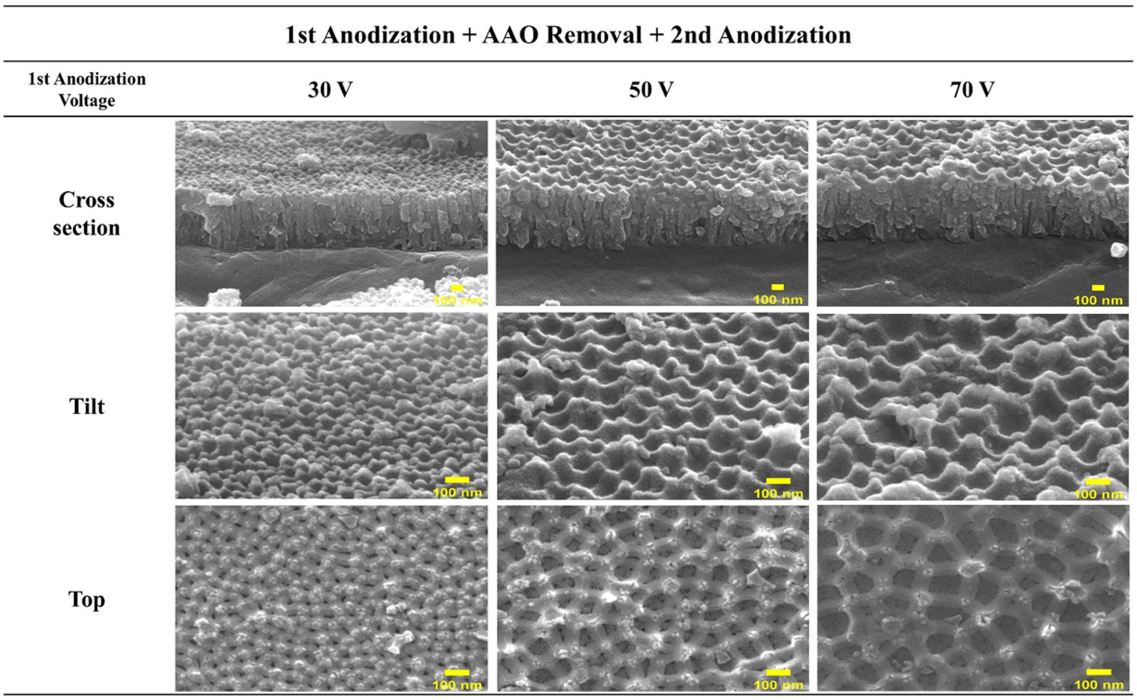

Fig. 2. The field emission–scanning electron microscopy (FE-SEM) images show the oxide film produced through modulation of the first anodization voltage, followed by the second anodization after the removal of the anodic aluminum oxide (AAO) layer

Table 1. Chemical composition of 6061 aluminum (Al) alloy

At%			
Al K	O K	Mg K	Si K
80.98	5.59	1.24	0.65

$$2Al^{3+} + 3O^{2-} \rightarrow Al_2O_3 \quad (1)$$

Following AAO removal, the second anodization process was conducted to observe the surface and thickness of the resulting oxide film structures and investigate the roughness, contact angle, and corrosion characteristics. The chemical composition of the untreated 6061 Al alloy used in the study was analyzed using EDS and is presented in Table 1. Fig. 2 shows the observation of the oxide film and nanopores formed through the second anodization process, as observed through FE-SEM. The thickness of the final oxide film, pore diameter (D_p), interpore distance (D_{int}), and solid fraction were measured and are reported in Table 2. The thickness of the final oxide film after the second anodization process grew to 571.94 ± 12.31 nm at 30 V, 652.83 ± 16.17 nm at 50 V, and 661.41 ± 27.76 nm at 70 V. Notably, the thickness of the final oxide film formed during the first anodization varied, with the thinnest film observed at an applied voltage of 30 V and the thickest at 70 V. This phenomenon can be attributed to the increased ion mobility as the anodization voltage increases, leading to more vigorous reactions and the formation of larger-diameter pores. Subsequently, removing these oxide films resulted in a residual pore pattern on the material's surface, exhibiting a wider pore diameter. Accordingly, the pore pattern formed at higher applied voltages results in a larger surface area, leading to a more extensive reaction when subjected to the same conditions as the second anodization. Thus, the final oxide film is thickest for samples subjected to the first anodization at 70 V because

Table 2. Thickness, pore diameter, interpore distance, and solid fraction of the final oxide film with first anodization voltage change

1st Anodization voltage (V)	Thickness (nm)	D_p (nm)	D_{int} (nm)	Solid Fraction
30	571.94 ± 12.31	20.13 ± 3.14	69.79 ± 8.94	0.9245
50	652.83 ± 16.17	75.82 ± 16.44	125.78 ± 15.35	0.6705
70	661.41 ± 27.76	133.18 ± 19.45	146.38 ± 15.68	0.2493

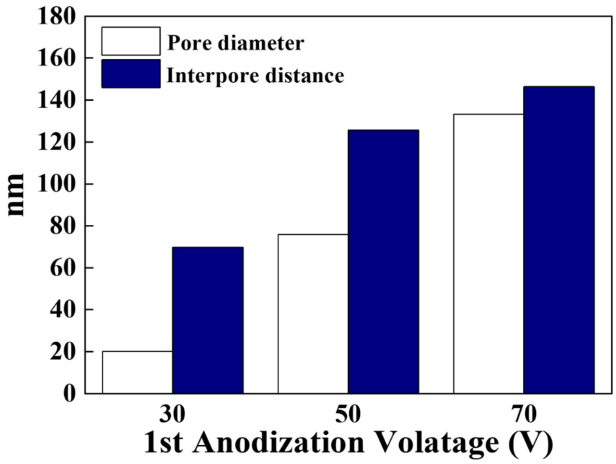

Fig. 3. Changes in the final pore diameter and interpore distance formed by modulating the first anodization voltage

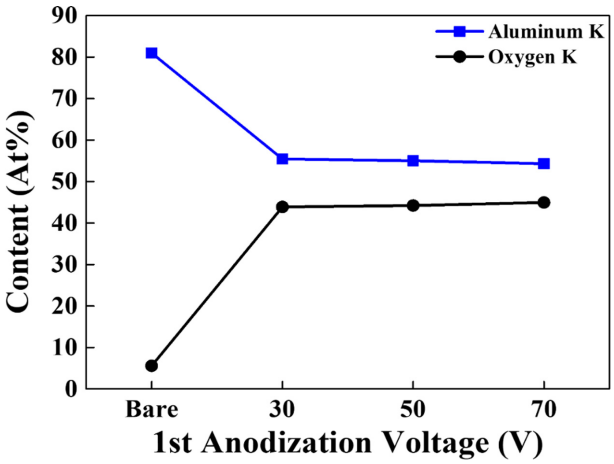

Fig. 4. Oxygen and aluminum content graph of the final oxide film with first anodization voltage change

of the broader reaction area during the subsequent second anodization.

The pore sizes of the resulting final oxide films corresponded to the applied voltage for the first anodization, with values of 20.13 ± 3.14 nm, 75.82 ± 16.44 nm, and 133.18 ± 19.45 nm for 30, 50, and 70 V, respectively. Similarly, the interpore distances are 69.79 ± 8.94 nm, 125.78 ± 15.35 nm, and 146.38 ± 15.68 nm. The pore size and interpore distance increase with higher first anodization voltages, as illustrated in Fig. 3. As pores widen, the thickness of the pore walls decreases. Consequently, the solid fraction of the final oxide film diminishes as the applied first anodization voltage increases, declining from 0.9245 to 0.2493. The solid fraction (f_{SL}) is calculated using equation (2), where "a" is the interpore distance and "r" is the pore radius.

$$f_{SL} = 1 - \frac{2\pi r^2}{\sqrt{3}a^2} \quad (2)$$

Table 3 summarizes the oxide film's chemical composition and content analysis based on variations in applied voltage during the first anodization, as analyzed using EDS. The compositional analysis revealed the presence of Al and O as the major components of the oxide film, with trace amounts of Mg and Si originating from the 6061 Al alloy. Fig. 4 presents the Al and O content changes for untreated samples and those subjected to anodization at different voltages. The anodized samples exhibited a decrease in Al content and a concurrent increase in O content compared to the untreated samples. This shift in chemical composition, as depicted by the reduction of Al content and the rise in O content, indicates the growth of the anodized oxide film, as O released at the cathode during anodization reacts with Al at the anode, leading to Al consumption and oxide film formation.

Table 3. Energy dispersive spectroscopy (EDS) component and content of the final oxide film formed with the first anodizing voltage change

1st Anodization Voltage (V)	At%			
	Al K	O K	Mg K	Si K
30	55.44	43.89	0.35	0.31
50	55.02	44.22	0.38	0.38
70	54.30	44.95	0.30	0.44

3.2 Roughness and wettability measurement

The surface roughness of the final oxide film was measured using AFM with respect to the varying first anodization voltages. The corresponding images and the average surface roughness value (R_a) are presented in Fig. 5 and detailed in Table 4, respectively. At the first anodization voltages of 30, 50, and 70 V, average surface roughness values were 41.64, 108.8, and 109.1 nm, respectively. This trend indicates that higher voltages result in increased surface roughness. The first anodization at lower voltages resulted in smaller and more uniformly distributed pore diameters, leading to lower surface roughness. Conversely, the formed oxide film exhibited larger and less uniform pore diameters

Table 4. R_a value of surface roughness of the final oxide film with first anodization voltage change

1st Anodization Voltage (V)	R_a
30	41.64
50	108.8
70	109.1

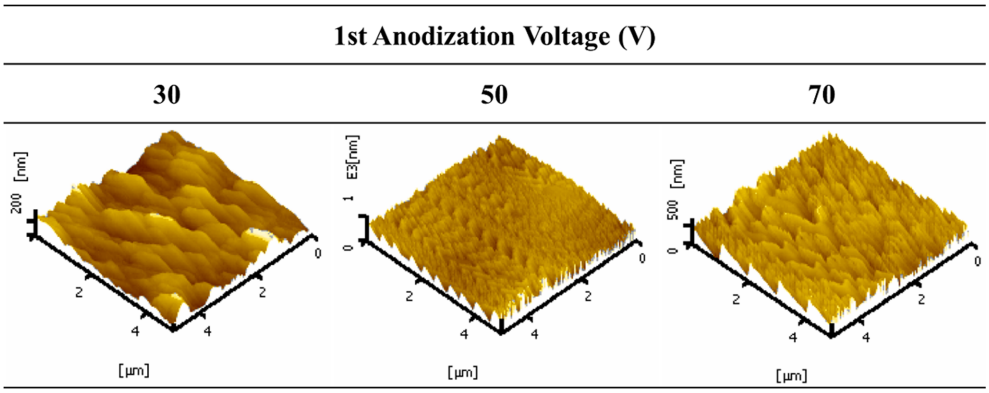

Fig. 5. Surface roughness of the final oxide film with first anodization voltage change

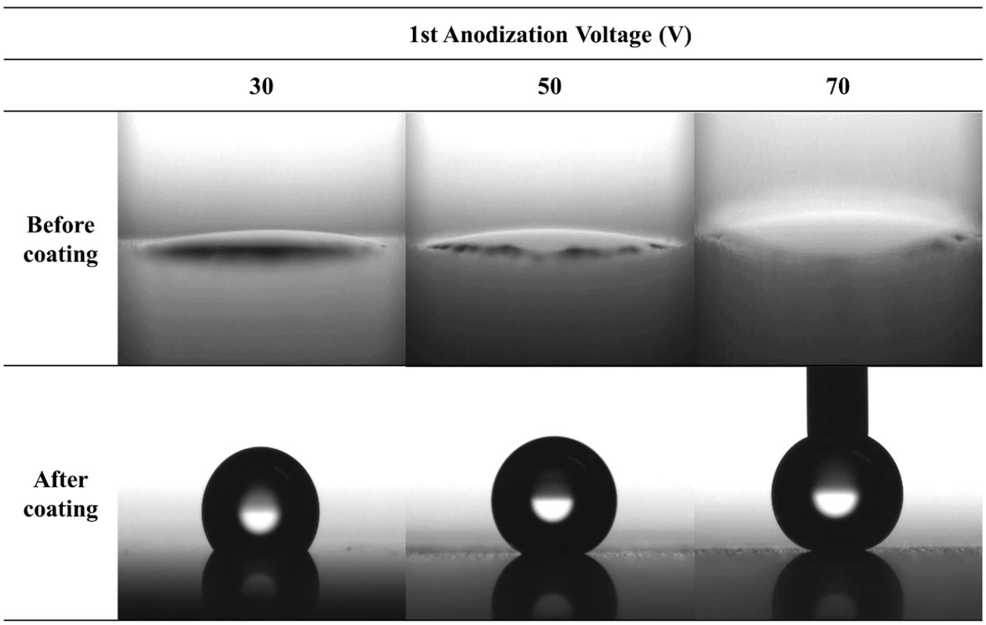

Fig. 6. Contact angle images of the surface before and after coating of the final oxide film with first anodization voltage change

at higher voltages, contributing to higher surface roughness.

In addition, Fig. 6 and Table 5 present the images and contact angle measurements before and after surface modification (SAM coating) for the samples with the final oxide films formed at different first anodization voltages. Before coating, rapid liquid spreading due to the pores in the oxide film led to apparent superhydrophilicity, rendering contact angle measurements unfeasible. Moreover, a direct relationship was observed between the pore diameter and the rapid liquid spreading. After coating, the contact angles were measured as 124.52° ± 11.66°, 165.32° ± 11.60°, and 178.36° ± 1.20° for the samples corresponding to 30 V, 50 V, and 70 V, respectively. These values indicate that the 30 V sample exhibited a hydrophobic surface, while the 50 V and 70 V samples achieved superhydrophobic surfaces. As the first anodization voltage increases, pore size expands, leading to thinner pore walls and decreased solid fraction. The coating on a surface with a lower solid fraction results in a smaller contact area between the surface and the liquid. Air trapped inside the pores prevents the liquid from spreading, creating a shape resembling air pockets within the pores.

Table 5. Water contact angles before and after coating the final oxide film with first anodization voltage change

1st Anodization Voltage (V)	Contact Angle (°)	
	Before coating	After coating
30	None	124.52 ± 11.66
50	None	165.32 ± 11.60
70	None	178.36 ± 1.20

Consequently, the sample with the largest pore size under the 70 V voltage condition exhibited the highest contact angle.

3.3 Polarization measurement

Meanwhile, Fig. 7 illustrates the polarization curves obtained from potentiodynamic polarization tests to compare the final anodized film's corrosion resistance under different anodization voltages. Table 6 presents the corrosion current density (I_{corr}) and corrosion potential (E_{corr}) determined using the Tafel extrapolation method. These values serve as electrochemical indicators for evaluating the polarization curves. As the mass loss indicating corrosion increases, the corrosion current density tends to increase while the corrosion potential decreases—corrosion resistance was inversely related to corrosion current density and directly related to corrosion potential. As the first anodization voltage increased, the corrosion current density rose from 5.07×10^{-7} A/cm^2 to 4.94×10^{-6} A/cm^2, while the corrosion potential dropped from +217.121 mV to +30.665 mV. Hence, the conditions of a 30 V first anodization voltage, with the lowest current density and highest corrosion potential, indicate excellent corrosion resistance attributed to the formation of the smallest pores that hinder the penetration of corrosive substances. On the other hand, under the conditions of a 70 V first anodization voltage, despite having the thickest oxide layer, lower corrosion resistance was observed because of larger pores and a wider surface area.

Moreover, Fig. 8 illustrates the polarization curves of samples with hydrophobic coatings applied to the final oxide layers, showing the effect of anodization voltage variation. Meanwhile, the corrosion current density and potential for these polarization curves are presented in Table 7. In the hydrophobically coated samples, as the anodization voltage increased, the corrosion current density decreased from 1.51×10^{-7} A/cm^2 to 1.94×10^{-8} A/cm^2, while the corrosion potential increased from +296.816 mV to +477.207 mV. Therefore, the condition of 70 V for the first anodization voltage exhibited the best corrosion resistance, as evidenced by the lowest corrosion current density and highest corrosion potential—attributed to the hydrophobic surface created by coating the structure with the lowest solid fraction, effectively preventing the penetration of Cl ions and inhibiting corrosion.

The results of the potentiodynamic polarization test, showing the corrosion current density graphs of the samples

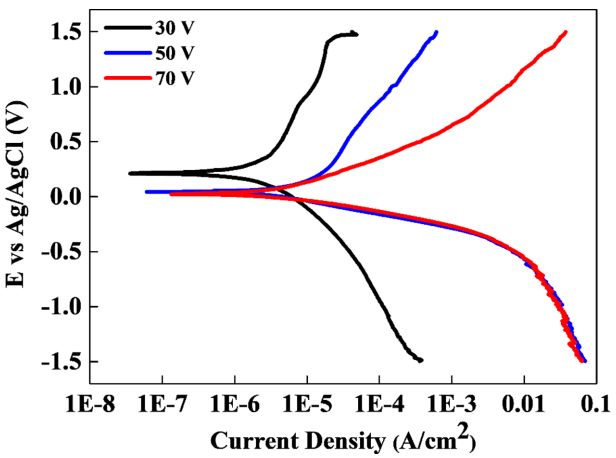

Fig. 7. Potentiodynamic polarization curves before coating of the final oxide film with first anodization voltage change

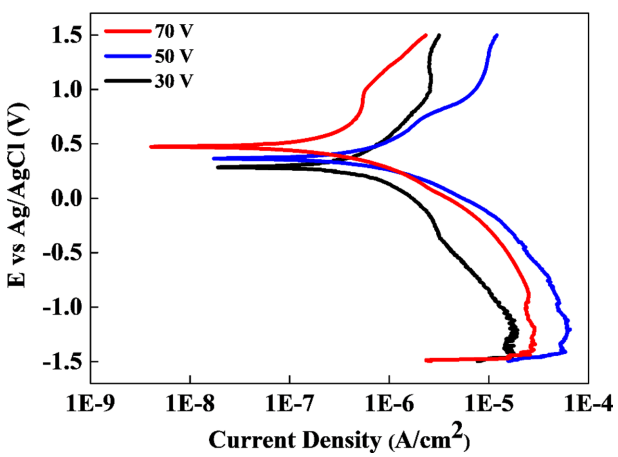

Fig. 8. Potentiodynamic polarization curves after coating of the final oxide film with first anodization voltage change

Table 6. Potentiodynamic polarization test results for oxide film with first anodization voltage change before coating

Before coating		
1st Anodization Voltage (V)	E_{corr} (mV)	I_{corr} (A/cm^2)
30	217.121	5.07×10^{-7}
50	50.100	6.69×10^{-7}
70	30.665	4.94×10^{-7}

Table 7. Potentiodynamic polarization test results for oxide film with first anodization voltage change after coating

After coating		
1st Anodization Voltage (V)	E_{corr} (mV)	I_{corr} (A/cm^2)
30	296.816	1.51×10^{-7}
50	371.573	1.07×10^{-7}
70	477.207	1.94×10^{-8}

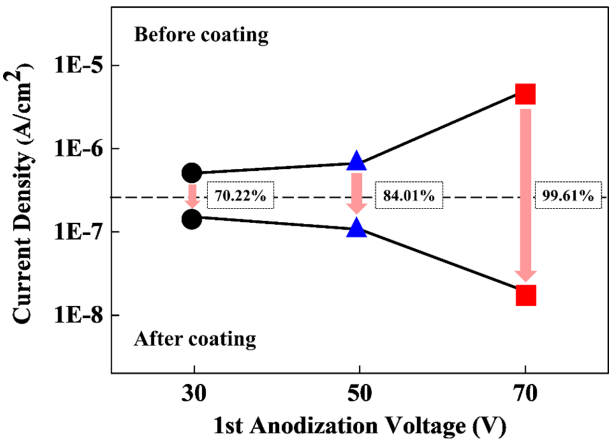

Fig. 9. Comparison graph of corrosion current density reduction rate before and after coating of final oxide film with first anodization voltage change

before and after coating, are presented in Fig. 9. The corrosion reduction rate was calculated using equation (3), where I_0 represents the corrosion current density value of the sample before coating, and I represent the corrosion current density value of the sample after coating.

$$P_i(\%) = \frac{I_o - I}{I_o} \times 100 \quad (3)$$

The corrosion current density values before and after coating decreased by 70.22% for the 30 V voltage condition (from 5.07×10^{-7} A/cm^2 to 1.51×10^{-7} A/cm^2), 84.01% for the 50 V voltage condition (from 6.69×10^{-7} A/cm^2 to 1.07×10^{-7} A/cm^2), and 99.61% for the 70 V voltage condition (from 4.94×10^{-6} A/cm^2 to 1.94×10^{-8} A/cm^2). With the increase in the first anodization voltage, resulting in larger pore diameters, the superior hydrophobic characteristics were achieved under the 70 V voltage condition. Consequently, the corrosion current density reduction rate before and after coating demonstrated a direct relationship with higher first anodization voltages, improving corrosion resistance.

4. Conclusions

This study conducted a two-step anodization process on 6061 Al alloy by varying the first anodization voltage (30, 50, and 70 V). As the first anodization voltage increased, the pore diameter and interpore distance of the formed oxide film increased, and the thickness of the final oxide film was the highest when the first anodization voltage was set at 70 V. Meanwhile, the EDS analysis results indicated that anodized samples exhibited decreased Aluminum (Al) content and increased oxygen (O) content compared to the untreated samples, indicating the formation of the oxide film through the anodization process. AFM measurements of oxide film surface roughness revealed that a higher first anodization voltage resulted in larger and more uneven pore structures, leading to increased surface roughness.

Moreover, all uncoated samples exhibited superhydrophilic behavior due to the pores formed in the oxide film, allowing the liquid to spread rapidly. After coating, the samples exhibited different wetting behaviors based on the first anodization voltage. When the solid fraction is low, the surface area in contact with the liquid is small when coated and hydrophobicity is maximized, so the 30V sample showed a hydrophobic surface, while those at 50 V and 70 V had superhydrophobic surface.

Furthermore, potentiodynamic polarization test results before coating, the 30 V sample had the best corrosion resistance due to reduced penetration of corrosive substances due to the small pore size. In the coated samples, it was observed that the best corrosion resistance was achieved for the 70 V first anodization condition, where a low solid fraction resulted in a superhydrophobic surface after coating.

The corrosion current density of the before and after coating samples decreased by 70.22% in the 30 V sample and 84.01% in the 50 V sample, and the 70 V sample showed the greatest improvement in corrosion resistance with a reduction rate of 99.61%. Therefore, conducting further research on process conditions is essential by applying appropriate voltages during the anodization process and controlling the coating application. This approach will facilitate the development of surface treatment technology (anodization) for aluminum alloy, meeting the requirements of the automotive, construction, shipbuilding, and marine industries. The optimization of process parameters remains crucial to ensure that the resulting materials possess the desired properties and corrosion resistance for practical applications.

Acknowledgments

The authors thank Subin Park, a student at Dong-eui University, for helping with the experiment.

References

1. C. Jeong, J. Lee, k. Sheppard and C. H. Choi, Air-impregnated Nanoporous Anodic Aluminum Oxide Layers for Enhancing the Corrosion Resistance of Aluminum, *Langmuir*, **31**, 11040 (2015). Doi: https://doi.org/10.1021/acs.langmuir.5b02392
2. M. izmir and B. Ercan, Anodization of Titanium Alloys for Orthopedic Applications, *Frontiers of Chemical Sci-*

ence and Engineering, **13**, 28 (2019). Doi: https://doi.org/10.1007/s11705-018-1759-y

3. Y. Alivov M. Pandikunta S. Nikishin and ZY. Fan, The Anodization Voltage Influence on the Properties of TiO2 Nanotubes Grown by Electrochemical Oxidation, *Nanotechnology*, **20**, 225602 (2009). Doi: https://doi.org/10.1088/0957-4484/20/22/225602
4. Y. Park and C. Jeong, Comparison of Hydrophobicity and Corrosion Properties of Aluminum 5052 and 6061 Alloys After Anodized Surface Treatment, *Corrosion Science and Technology*, **21**, 200 (2022). Doi: https://doi.org/10.14773/cst.2022.21.3.200
5. C. Yao and T. J. Webster, Anodization: A Promising Nano-modification Technique of Titanium Implants for Orthopedic Applications, *Journal of nanoscience and nanotechnology*, **6**, 2682 (2006). Doi: https://doi.org/10.1166/jnn.2006.447
6. C. J. Donahue and J. A. Exline, Anodizing and Coloring Aluminum Alloys, *Journal of Chemical Education*, **91**, 711 (2014). Doi: https://doi.org/10.1021/ed3005598
7. C. Jeong, J. Jung, K. Sheppard and C. H. Choi, Control of the Nanopore Architecture of Anodic Alumina via Stepwise Anodization with Voltage Modulation and Pore Widening, *Nanomaterials*, **13**, 342 (2023). Doi: https://doi.org/10.3390/nano13020342
8. S. Lin, H. Greene, H. Shin and F. Mansfeld, Corrosion Protection of Al/SiC Metal Matrix Composites by Anodizing, *Corrosion*, **48**, 61 (1992). Doi: https://doi.org/10.5006/1.3315920
9. F. Nowruzi, R. Imani and S, Faghihi, Effect of Electrochemical Oxidation and Drug Loading on the Antibacterial Properties and Cell Biocompatibility of Titanium Substrates, *Scientific Reports*, **12**, 1 (2022). Doi: https://doi.org/10.1038/s41598-022-12332-z
10. Z. B. Xie, S. Adams, D. J. Blackwood and J. Wang, The Effects of Anodization Parameters on Titania Nanotube Arrays and Dye Sensitized Solar Cells, *Nanotechnology*, **19**, 405701 (2008). Doi: https://doi.org/10.1088/0957-4484/19/40/405701
11. W. J. Stepniowski and Z. Bojar, Synthesis of Anodic Aluminum Oxide (AAO) at Relatively High Temperatures. Study of the Influence of Anodization Conditions on the Alumina Structural Features, *Surfaces and Coatings technology*, **206**, 265 (2011). Doi: https://doi.org/10.1016/j.surfcoat.2011.07.020
12. H. Ji and C. Jeong, Systematic Control of Anodic Aluminum Oxide Nanostructures for Enhancing the Superhydrophobicity of 5052 Aluminum Alloy. *Materials*, **12**, 3231 (2019). Doi: https://doi.org/10.3390/ma12193231
13. C. C. Chen, W. D. Jehng, L. L. Li and E. W. G. Diau, Enhanced Efficiency of Dye-sensitized Solar Cells Using Anodic Titanium Oxide Nanotube Arrays, *Journal of the Electrochemical Society*, **156**, C304 (2009). Doi: https://doi.org/10.1149/1.3153288
14. L. Bouchama, N. Azzouz, N. Boumouche, J. P. Chopart, A. L. Daltin and Y. Bouznit, Enhancing Aluminum Corrosion Resistance by Two-Step Anodizing Process, *Surface and Coating Technology*, **235**, 676 2013). Doi: https://doi.org/10.1016/j.surfcoat.2013.08.046
15. Y. Kim and W. B. Kim, Enhancing the Surface Hydrophilicity of an Aluminum Alloy Using Two-Step Anodizing and the Effect on Inkjet Printing Characteristics, *Coatings*, **13**, 232 (2023). Doi: https://doi.org/10.3390/coatings13020232
16. X. Wang and G. R. Han, Fabrication and Characterization of Anodic Aluminum Oxide Template, *Microelectronic Engineering*, **66**, 166 (2003). Doi: https://doi.org/10.1016/S0167-9317(03)00042-X
17. J. S. Kim and C. Jeong, A Study on the Surface Properties and Corrosion Behavior of Functional Aluminum 3003 Alloy using Anodization Method, *Corrosion Science and Technology*, **21**, 209 (2022). Doi: https://doi.org/10.14773/cst.2022.21.4.290
18. C. C Chen, H. W. Chung, C. H. Chen, H. P. Lu, C. M. Lan, S. F. Chen, L. Luo, C. S. Hung and E. W. G. Diau, Fabrication and Characterization of Anodic Titanium Oxide Nanotube Arrays of Controlled Length for Highly Efficient Dye-Sensitized Solar, *The Journal of Physical chemistry C*, **112**, 19151 (2008). Doi: https://doi.org/10.1021/jp806281r
19. Y. Choi and C. Jeong, Influence of Electrolyte on the Shape and Characteristics of TiO_2 during Anodic Oxidation of Titanium, *Corrosion Science and Technology,* **22**, 193 (2023). Doi: https://doi.org/10.14773/cst.2023.22.3.193
20. T. Kikuchi, O. Nishinaga, S. Natsui and R. O. Suzuki, Fabrication of Self-ordered Porous Alumina via Etidronic Acid Anodizing and Structural Color Generation from Submicrometer-Scale Dimple Array, *Electrochimica Acta*, **156**, 235 (2015). Doi: https://doi.org/10.1016/j.electacta.2014.12.171
21. J. Zhao, X. Wang, R. Chen and L. Li, Fabrication of Titanium Oxide Nanotube Arrays by Anodic Oxidation, *Solid State Communications*, **134**, 705 (2005). Doi:

https://doi.org/10.1016/j.ssc.2005.02.028

22. W. J. Stepniowski, D. Zasada and Z. Bojar, First Step of Anodization Influences the Final Nanopore Arrangement in Anodized Alumina, *Surface and Coatings Technology*, **206**, 1416 (2011). Doi: https://doi.org/10.1016/j.surfcoat.2011.09.004
23. H. Ji and C. Jeong, Study on Corrosion and Oxide Growth Behavior of Anodized Aluminum 5052 Alloy, *Journal of the Korean Institute of Surface Engineering*, **51**, 372 (2018). Doi: https://doi.org/10.5695/JKISE.2018.51.6.372
24. J. Li, H. Wei, K. Zhao, M. Wang, D. Chen and M. Chen, Effect of Anodizing Temperature and Organic Acid Addition on the Structure and Corrosion Resistance of Anodic Aluminum Oxide Films, *Thin Solid Films*, **713**, 138389 (2020). Doi: https://doi.org/10.1016/j.tsf.2020.138359
25. Y. Huang, H, Shih, J. Daugherty. S. Wu, S. Ramanathan, C. Chang and F. Mansfeld, Evaluation of the Corrosion Resistance of Anodized Aluminum 6061 Using Electrochemical Impedance Spectroscopy (EIS), *Corrosion Science*, **50**, 3569 (2008). Doi: https://doi.org/10.1016/j.corsci.2008.09.008
26. Y. Zuo, P. H. Zhao and J. M. Zhao, The Influences of Sealing Methods on Corrosion Behavior of Anodized Aluminum Alloys in NaCl Solutions, *Surface and Coatings Technology*, **166**, 237 (2003). Doi: https://doi.org/10.1016/S0257-8972(02)00779-X
27. M. Mehdizade, M. Soltanieh and A. R. Eivani, Investigation of Anodizing Time and Pulse Voltage Modes on the Corrosion Behavior of Nanostructured Anodic Layer in Commercial Pure Aluminum, *Surface and Coatings Technology*, **358**, 741 (2019). Doi: https://doi.org/10.1016/j.surfcoat.2018.08.046
28. J. Lee, S. Shin, Y. Jiang, C. Jeong, H. A. Stone and C. H. Choi, Oil?Impregnated Nanoporous Oxide Layer for Corrosion Protection with Self?healing, *Advanced Functional Materials*, **27**, 1606040 (2017). Doi: https://doi.org/10.1002/adfm.201606040
29. L. Feng, H. Zhang, Z. Wang and Y. Liu, Superhydrophobic Aluminum Alloy Surface: Fabrication, Structure and Corrosion Resistance, *Colloids and Surfaces A: Physicochemical and Engineering Aspects*, **441**, 319 (2014). Doi: https://doi.org/10.1016/j.colsurfa.2013.09.014
30. M. Norek, M. Dopierala and W. J. Stepniowski, Ethanol Influence on Arrangement and Geometrical Parameters of Aluminum Concaves Prepared in a Modified Hard Anodization for Fabrication of Highly Ordered Nanoporous Alumina, *Journal of Electroanalytical Chemistry,* **750**, 79 (2015). Doi: https://doi.org/10.1016/j.jelechem.2015.05.024
31. G. X. Xiang, S. Y. Li, H. Song and Y. G. Nan, Fabrication of Modifier-Free Superhydrophobic Surfaces with Anti-Icing and Self-Cleaning Properties on Ti Substrate by Anodization Method, *Microelectronic Engineering*, **233**, 111430 (2020). Doi: https://doi.org/10.1016/j.mee.2020.111430
32. J. Zang, S. Yu, G. Zhu and X. Zhou, Fabrication of Superhydrophobic Surface on Aluminum Alloy 6061 by a Facile and Effective Anodic Oxidation Method, *Surface and Coatings Technology*, **380**, 125078 (2019). Doi: https://doi.org/10.1016/j.surfcoat.2019.125078
33. C. Jeong and C. H. Choi, Single-Step Direct Fabrication of Pillar-on-Pore Hybrid Nanostructures in Anodizing Aluminum for Superior Superhydrophobic Efficiency, *ACS applied materials & interfaces*, **4**, 842 (2012). Doi: https://doi.org/10.1021/am201514n
34. M. A. Hormozi, M. Yahoubi and M. E. Bahrololoom, A Facile Method for Fabrication of Hybrid Hydrophobic-Hydrophilic Surfaces on Anodized Aluminum Template by Electrophoretic Deposition, *Thin Solid Films*, **724**, 138597 (2021). Doi: https://doi.org/10.1016/j.tsf.2021.138597
35. H. Sakaue, T. Tabei and M. Kameda, Hydrophobic Monolayer Coating on Anodized Aluminum Pressure-Sensitive Paint, *Sensors and Actuators B: Chemical*, **119**, 504 (2006). Doi: https://doi.org/10.1016/j.snb.2006.01.010
36. Z. Wu, C. Richter and L. Menon, A Study of Anodization Process during Pore Formation in Nanoporous Alumina Templates, *Journal of the Electrochemical Society*, **154**, E8 (2006). Doi: http://doi.org/10.1149/1.2382671
37. C. Jeong, A Study on Functional Hydrophobic Stainless Steel 316L Using Single-Step Anodization and z Self-Assembled Monolayer Coating to Improve Corrosion Resistance, *Coatings*, **12**, 395 (2022). Doi: https://doi.org/10.3390/coatings12030395
38. W. Lee and S. J. Park, Porous Anodic Aluminum Oxide: Anodization and Templated Synthesis of Functional Nanostructures, *Chemical Reviews*, **114**, 7487 (2014). Doi: https://doi.org/10.1021/cr500002z